Author Manuscript

Author Manuscript

Author Manuscript

Author Manuscript

HHS Public Access

Author manuscript

*IEEE Trans Ultrason Ferroelectr Freq Control*. Author manuscript; available in PMC 2020 October 27.

Published in final edited form as:

*IEEE Trans Ultrason Ferroelectr Freq Control*. 2020 October ; 67(10): 2057–2068. doi:10.1109/TUFFC.2020.2998979.

# Parallel receive beamforming improves the performance of focused transmit based single track location shear wave elastography

**Rifat Ahmed [student member, IEEE]**, **Marvin M. Doyley [senior member, IEEE]**

Electrical and Computer Engineering, University of Rochester, NY, USA.

## Abstract

Single track location shear wave elastography (STL-SWEI) is robust against speckle-induced noise in shear wave speed (SWS) estimates, however it is not immune to other incoherent sources of noise (such as electronic noise) that increase the variance in SWS estimates. Although estimation averaging enabled by parallel receive beamforming adequately suppresses these noise sources, these beamforming techniques often rely on broad transmit beams (plane or diverging). While broad beam approaches such as plane wave imaging are becoming ubiquitous in research ultrasound systems, clinical systems usually employ focused transmit beams due to compatibility with hardware beamforming and deeper penetration. Consequently, improving the noise robustness of focused transmit based STL-SWEI may enable easier translation to clinical scenarios. In this work, we experimentally evaluated the performance of parallel beamforming for STL-SWEI using fixed or multiple transmit focus. By imaging tissue-mimicking phantoms, we found that parallel beamforming improved the focal zone elastographic signal-to-noise ratio ($SNR_e$) by 40.9%. For a receive line spacing equivalent to transducer pitch, averaging estimates from three parallel lines produced peak $SNR_e$ at the focal zone (25 mm) while at the shallower regions (<20 mm) a larger number of parallel lines (>7) were needed. Increasing the beamforming line density by a factor of 8 increased the focal zone $SNR_e$ only by 13.2%. When SWS quantification was desirable at a fixed depth (such as within the push focal depth), using a deeper tracking focal zone enabled higher parallel line count and improved the peak $SNR_e$ by 33%. The multi-focusing strategy produced a lower $SNR_e$ than the single focus configurations. For a fixed tracking focal zone, a depth-dependent averaging based on simulated transmit intensity adequately accounted for the transmit beamwidth. The results in this work demonstrated that STL-SWEI can be implemented using focused transmit beams with robust noise-suppression capability.

### Keywords

Shear wave elastography; single track location; beamforming; focused transmit

## II. Introduction

Shear wave elasticity imaging (SWEI) [1], [2], [3] has shown promising results for the assessment of liver fibrosis [4] and cancer detection [5], [6]. SWEI quantifies soft tissue stiffness which contains potential diagnostic information. It uses acoustic radiation force to induce shear wave propagation in tissue. By using ultrasound beamforming techniques,

Author Manuscript Author Manuscript Author Manuscript Author Manuscript

SWEI tracks the propagation of shear wave and estimates the shear wave speed (SWS) which is directly related to tissue stiffness.

The conventional approaches to SWEI produce noisy estimates of SWS due to the speckle-induced uncertainties in shear wave arrival time estimates [7], [8]. In SWEI, the SWS is estimated by measuring the shear wave arrival times at two or multiple lateral locations. McAleavey *et al.* demonstrated that the random nature of ultrasound speckle introduces an uncertainty on the location where the arrival time estimates register and, consequently, produces spatially noisy SWS estimates [8]. Although larger processing kernels or spatial filtering can diminish this effect, they also degrade the image resolution of SWEI. Thus, the ultrasound speckle introduces a resolution versus noise tradeoff in SWEI [7]. Single-track location SWEI (STL-SWEI) [9] overcomes this tradeoff by using multiple lateral shear wave sources and tracking waves at a fixed location. While STL-SWEI can potentially image with lower spatial noise and improved resolution, it is not immune to other sources of noise including thermal noise. Low sonographic signal-to-noise ratio ($SNR_s$) increases the variance in SWS estimates provided by STL-SWEI.

Beamforming techniques enable robust noise suppression in SWEI. In traditional multiple-track location SWEI (MTL-SWEI), parallel receive beamforming techniques are often used to track shear wave propagation at multiple lateral locations simultaneously. When combined with broad beam transmission techniques such as plane wave imaging [10], parallel receive beamforming allows rapid acquisition (< 50 ms) of MTL-SWEI. Consequently, these beamforming techniques enable robust noise suppression through multiacquisition averaging [11]. Although parallel beamforming does not reduce the acquisition time of STL-SWEI, it may still enable noise suppression through a different mechanism. For example, shear waves from a pair of push pulses can be simultaneously tracked at multiple locations which may provide redundant SWS estimates in STL-SWEI. By averaging these redundant estimates, significant reduction in SWS variance was previously achieved [12], [7], [13], [14], [15], [16], [17]. We recently showed that the variance of SWS reduces as a function of parallel receive line count [16].

Ultrasound beamforming with large parallel receive count typically requires wider transmit beams in order to ensure overlap between transmit and receive beams. Consequently, plane [16], [17], [7] or diverging waves [15], [14] have been utilized in STL-SWEI for noise suppression. Although open ultrasound platforms [18] with higher computational resources (large buffer memory, software beamforming) have made the wide transmit beams (plane or diverging) ubiquitous in research laboratories, many clinical scanners still rely on focused transmit beams due to compatibility with prevalent hardware beamforming architectures. Focused transmit beams also enable deeper penetration and higher $SNR_s$ than synthetic focusing techniques, especially when the number of transmit pulses are fewer. For example, the frame rate of SWEI allows only a few angular transmits (3-7 depending on imaging depth and application) in compounded plane wave (CPW) imaging [10], which limits the $SNR_s$ of CPW in this application [19]. Despite these limitations of CPW in SWEI, we previously found that CPW imaging outperformed focused imaging in STL-SWEI due to parallel track line averaging (>10) [16]. In this work, we hypothesize that by using parallel receive beamforming with focused transmits, it may be possible to significantly enhance the

Author Manuscript Author Manuscript Author Manuscript Author Manuscript

performance of focused STL-SWEI. Improving the performance of focused STL-SWEI may enable faster translation to clinical systems.

The goal of this paper is to assess the impact of parallel beamforming strategies, using focused tracking beams, on the quality of SWS estimates provided by STL-SWEI. We evaluated single and multi-focusing approaches to investigate the depth-dependent performance of STL-SWEI. We experimentally investigated different approaches that can maximize the performance of parallel beamforming in STL-SWEI within the constraints imposed by the shape of focused transmit beams. We evaluated the efficacy of these approaches in homogeneous and heterogeneous tissue-mimicking phantoms.

## III. Methods

### Parallel beamformed STL-SWEI with single and multi-focused tracking

**Pulse sequences:** In this work, we implemented STL-SWEI with focused tracking transmits and parallel receive beamforming (fig. 1(a)). We used a total of 20 pairs of push beams with a distance of 0.3 mm between pairs. Within each pair, push beams were separated by 1.2 mm (ΔP in fig. 1(a)). Within each pair, an identical set of focused track beams were transmitted followed by each push beam. Since the required frame rate of SWEI (~2-3 kHz) was less than the pulse repetition frequency (PRF) of tracking pulses (12 kHz in this study), we utilized four consecutive transmit pulses to synthesize a tracking receive frame. We investigated two different strategies to transmit these 4 pulses. One strategy (single focus) used a fixed transmit focus (25 mm, unless otherwise specified) and transmit aperture for all four pulses (fig. 1b). In the other strategy (multi-focus), the four pulses had an identical beam axis, but each beam was focused at gradually increasing depths (10, 15, 20 and 25 mm) with a constant transmit F# (focal depth/aperture size) of 2.0 (fig. 1c). Track beams were transmitted to the left of the push pulses and the distance between the push (the left one in a push-pair) and track beam axes was maintained at 6 mm (ΔT in fig. 1(a)) for all pairs of push beams. Consequently, the absolute position of the track beam changed from one push-pair to the next (fig. 1(a)).

**Data acquisition and beamforming:** We acquired all data in this study using a research ultrasound system (Vantage 256, Verasonics Inc. , Kirkland, WA, USA) equipped with an L11-5v probe. We used 5 MHz pulses for push beams and 10 MHz pulses for tracking beams. Push beams were 400 μs in duration and were focused at 25 mm depth. During tracking receive, data was acquired using all 128 transducer elements.

We used the pixel-oriented processing provided by Verasonics [20] to produce parallel receive lines with geometric focusing. From each tracking transmit pulse, we beamformed 15 (unless otherwise specified) parallel lines as inphase/quadrature (IQ) data. Receive beamforming was performed using dynamic-receive aperture growth. The pixel-oriented processing in Verasonics achieves aperture growth through the specification of element angular sensitivity which is an alternative description of receive aperture F#. Specifically, the receive aperture was limited to elements whose angular sensitivity was higher than −3 dB (empirically determined) at the beamforming pixel. Consequently, the effective receive aperture changed from one parallel line to the next at any given depth and was centered

Author Manuscript Author Manuscript Author Manuscript Author Manuscript

around the beamformed line. The receive lines were symmetrically distributed around the transmit beam axis with a 0.3 mm line spacing (equal to the transducer pitch) unless otherwise specified.

For both single and multi-focus sequences, parallel beamformed IQ lines from four consecutive temporal pulses were coherently added (compounded). For the multi-focus sequences, the compounding resulted in synthetic transmit focusing. For the single focus sequence, the compounding ensured a similar temporal averaging compared to multi-focal sequences and plane wave STL-SWEI (described next). Compounding was performed in a sliding window manner.

### Plane wave based STL-SWEI

The STL-SWEI methods with focused parallel beamforming were compared to plane wave based STL-SWEI (pSTL-SWEI) [16]. The pSTL-SWEI sequence was identical to the focused STL-SWEI sequences except the focused pulses were replaced with angular plane wave transmissions (fig. 1d). We transmitted 4 plane wave angles (−1.5°, −0.5°, 0.5° and 1.5°; chosen from a prior optimization study [19]) followed by each push pulse. A total of 15 IQ lines (comparable to a previous study [16]) were beamformed from each plane wave and the lines from 4 pulses were temporally compounded in a sliding window manner.

### Shear wave speed reconstruction

We used a 2D auto-correlation method to estimate the wave motion from the IQ stack corresponding to each push-detect ensemble [21]. Shear wave traces through the slow time were bandpass filtered (band-limited between 50 Hz and 1 kHz). For a pair of push-detect events, shear wave arrival time delay was estimated at a fixed track position using a GPU-accelerated cross-correlation method [22]. The ratio of push-beam distance (ΔP) and the time delay provided the SWS. For a given pair of push beams, SWS was reconstructed at N (varied from 1 to 15) parallel positions. The final SWS at a given location was estimated as the weighted average of all N estimates. The square of the cross-correlation coefficients between the wave profiles was used as the averaging weight [16].

### Depth-dependent averaging for focused imaging

Due to large parallel receive count, beamformed lines were often positioned outside the transmit beam particularly at the focal zone. Although it is possible to beamform a pixel outside the transmit beam using a spherical delay model [23], such lines contain poor $SNR_s$. Consequently, to improve the effectiveness of parallel receive beamforming, we developed an approach to perform depth-dependent averaging (DDA). In this approach, we only averaged SWS estimates that were obtained from track lines within the lateral extent of the transmit beamwidth. To achieve this, at each depth, the number of parallel track lines or, equivalently, the size of the averaging set was selected from a pre-defined profile (DDA profile) which was computed from a transmit intensity simulation. To obtain the DDA profile, we used the ultrasound simulation tool FIELD II [24] to model the L11-5v transducer. Next, we simulated the transmit pressure field using the transmit F#, focal depth, and tissue attenuation coefficient ($\alpha_A$) as inputs. Log-normalized intensity was computed from the transmit pressure field. We then used a contour threshold to estimate the lateral

Author Manuscript Author Manuscript Author Manuscript Author Manuscript

beamwidth at each depth. The depth-dependent lateral beamwidth profile was then divided by the beamforming line density (0.3 mm) to obtain the DDA profile that indicated the maximum number of parallel lines at each depth. An upper limit of 15 parallel lines at any depth was set to match the experimental condition.

We determined the intensity contour threshold using a heuristic approach. Specifically, we acquired fixed-focus STL-SWEI data from a homogeneous elastic phantom with an acoustic attenuation of 0.5 dB/cm/MHz. SWS maps were reconstructed using these data with varying levels of track line averaging (1 to 15, in steps of 2). For each elastogram, a 1 mm axial kernel was used to compute the depth-dependent elastographic signal-to-noise ratio ($SNR_e$) (defined in the next section). At any given depth, the averaging level that maximized that $SNR_e$ was evaluated. Repeating this process at all depths produced a depth-dependent optimum $SNR_e$ profile and a corresponding depth-dependent optimum averaging profile. This optimum averaging profile was compared against the DDA profiles obtained using −6 dB, −9 dB, −12 db, and −15 dB contours of the transmit intensity. The −12 dB contour was used as the DDA profile. For phantoms with unknown acoustic attenuation coefficient, we assumed an $\alpha_A$ = 0.5 dB/cm/MHz to perform the DDA.

For the multi-focus sequences, the DDA profile was applied to the IQ data prior to coherent compounding. Specifically, the DDA profile was computed using a −12 dB contour threshold for each of the pulses with different transmit focus. Then, the lateral extent to the parallel receive lines were limited within the contour. After applying these lateral masks, the beamformed IQ lines from each of the pulses were coherently compounded.

## Performance evaluation

We used the elastographic signal-to-noise ratio ($SNR_e$) performance metric to evaluate SWS elastograms, defined as follows:

$$SNR_e = \frac{\mu}{\sigma} \tag{1}$$

where $\mu$ represents the mean SWS in an elastically homogeneous region of the tissue, and $\sigma$ represents the variance of SWS values within the region.

For all homogeneous phantoms, we evaluated $SNR_e$ as a function of depth. To achieve this, we divided the entire elastograms into overlapping 1 mm axial segments with 0.5 mm overlap. By computing $SNR_e$ in each of the axial segments, we obtained a depth-dependent $SNR_e$. When $SNR_e$ was analyzed at specific depths, a larger 5 mm axial kernel was used.

We used the elastographic contrast-to-noise ratio ($CNR_e$) performance metric to assess lesion detectability, defined as follows:

$$CNR_e = \frac{|\mu_L - \mu_B|}{\sqrt{\sigma_L^2 + \sigma_B^2}}, \tag{2}$$

Author Manuscript Author Manuscript Author Manuscript Author Manuscript

where $\mu_L$ and $\mu_B$ represent the mean SWS in the lesion and background material, respectively; $\sigma_L$ and $\sigma_B$ represent the standard deviation of SWS in the lesion and background material, respectively.

## Phantom Study

We performed different studies using a commercially available multi-purpose phantom (Model 04GSE, CIRS Inc., Norfolk, VA, USA). The phantom had two elastically homogeneous regions with different acoustic attenuation coefficients ($\alpha_A$ = 0.5 dB/cm/MHz and 0.7 dB/cm/MHz). The phantom also contained a cylindrical elastic inclusion which was softer than the background. Additionally, we used a CIRS homogeneous viscoelastic phantom (Serial#: 2095.1-1 (custom), shear attenuation: 0.606 ± 0.063 $Npmm^{-1}$ $kHz^{-1}$ [25]). We performed all parametric studies on the homogeneous elastic phantom with $\alpha_A$ = 0.5 dB/cm/MHz. The comparison studies between focused and plane wave tracking were performed on all phantoms. Following experiments were conducted:

**A. Evaluating the effect of focused aperture configuration and level of averaging:** To understand the effect of transmit aperture configuration and the level of averaging on the performance of focused STL-SWEI, we performed studies on a homogeneous elastic phantom ($\alpha_A$ = 0.5 dB/cm/MHz) using single focus sequences with different transmit F#. The transmit F# was varied from 1.5 to 5.0 in steps of 0.5. For each value of the F#, we evaluated the depth-dependent $SNR_e$ of the SWS maps obtained using different levels of parallel line averaging.

**B. Evaluating the impact of track line spacing on focused parallel beamforming:** Because the beamwidth of focused transmission only allows a limited number of track lines at the focal zone, we evaluated the effectiveness of beamforming with smaller line spacing. We acquired data from a homogeneous phantom ($\alpha_A$ = 0.5 dB/cm/MHz) with four different beamforming line densities (1, 2 4, and 8 lines per transducer pitch). Since the densely beamformed configurations can accommodate more parallel lines than the sparse ones, we beamformed 49 parallel track lines from each transmit pulse for this particular study.

**C. Evaluating the impact of using a focal zone deeper than the region of interest (ROI):** In SWEI, quantification is often performed within a ROI at a fixed depth (such as push focal depth). We evaluated whether $SNR_e$ improves when the tracking focal zone is placed deeper than the ROI. We performed this experiment on a homogeneous elastic phantom ($\alpha_A$ = 0.5 dB/cm/MHz). We acquired data with push focus at 15 mm while we varied the track focal zone (15, 20, 25, and 30 mm). In each configuration, we estimated SWS with different levels of track line averaging (1 to 15 in steps of 2). The $SNR_e$ was evaluated at the constant focal depth of the push beam (15 mm).

**D. Comparison of plane wave and focused sequences:** We compared the focused STL-SWEI and pSTL-SWEI on the three homogeneous phantoms. We compared fixed focus STL without averaging and with DDA against pSTL-SWEI with 15 track line averaging.

Author Manuscript Author Manuscript Author Manuscript Author Manuscript

**E. Evaluating the lesion detectability:** We used a CIRS phantom (model 04GSE) with a cylindrical inclusion to evaluate the lesion detectability of the proposed methods. The inclusion was softer than the background and was 6 mm in diameter. We evaluated single focus STL-SWEI with 1, 3, 5, 7, 11, and 15 track line averaging and DDA, and pSTL-SWEI with 15 track line averaging. Since the measurements were performed within the fixed depth of the inclusion, we evaluated two different tracking foci: one approximately at the center of the inclusion (15 mm) and one at a region deeper than the inclusion (25 mm). For all experiments on the inclusion phantom, the push focal zone was set at 15 mm and a total of 40 push-pairs were utilized to widen the field-of-view of the elastograms.

## IV. Results

### Shear wave speed maps reconstructed at off-axis track positions were noisier than those at on-axis track positions (fig. 2).

For the single focus sequences, the focal zone $SNR_e$ was highest when the receive beam was aligned with the transmit beam axis, and the $SNR_e$ gradually decreased where the receive beam position was offset from the beam axis (fig. 2(a),(c)). At the shallow regions (<15 mm), $SNR_e$ was similar for all receive beam positions (fig. 2(c)). For the multi-focus sequence, the $SNR_e$ decayed relatively gradually over depth (fig. 2(d)). At any given depth, the $SNR_e$ decreased when the receive beam moved away from the transmit beam axis. Except at the shallow depths (<15 mm) in the central receive lines (within approximately 0.6 mm of beam axis), the depth-dependent $SNR_e$ was comparatively lower in the multi-focal sequence than the single focus sequence for any given receive position.

### DDA compensates for transmit beamwidth and yields depth-dependent optimum performance in single-focus imaging (fig. 3).

The number of parallel lines required to achieve optimum $SNR_e$ at each depth followed the −6 to −15 dB transmit beam contours (fig. 3c). Additionally, there was a large discrepancy in the near-field (<10 mm) between the simulated contours and the one achieved through SWEI experiment. Despite the depth-dependent variation in optimum contour threshold values, when using a −12 dB threshold, the depth-dependent $SNR_e$ approximated the optimum depth-dependent $SNR_e$ for all three homogeneous phantoms (fig. 3(d)-(f)).

### Multi-focusing strategies did not provide better depth-dependent performance than single focus imaging (fig. 4).

In the single focus case, $SNR_e$ increased as a function of parallel line count at depths shallower than 18 mm (fig. 4a). At depths beyond 18 mm, DDA was necessary to optimize the depth-dependent $SNR_e$. For multi-focal imaging, noise increased uniformly over depths beyond the first focus (>10 mm) when more than three (often five) parallel SWS estimates were averaged (fig. 4b). Using seven or more parallel lines resulted in severe degradation in $SNR_e$. DDA was not effective in multi-focus sequences. Specifically, at depths beyond 10 mm, $SNR_e$ produced by DDA gradually decayed over depth. Single focus imaging produced higher $SNR_e$ than multi-focus imaging. For example, when compared against the depth-wise best performance of multi-focus imaging, the DDA of single focus imaging produced 14.6 to 102.1% higher $SNR_e$ (within 10 to 25 mm range).

Author Manuscript Author Manuscript Author Manuscript Author Manuscript

**Increasing the line density of parallel receive beamforming marginally improved the $SNR_e$ at the expense of increased parallel line counts (fig. 5).**

When the receive line density of single-focus sequence was increased by a factor of 2, 4, and 8, the peak $SNR_e$ in the focal region improved by 2.3, 7.5, and 13.2%, respectively (fig. 5(c)). However, to achieve these peak $SNR_e$, the parallel lines used in the SWS averaging also increased from 3 to 5, 11, and 27, respectively. In the shallow region (15mm), peak $SNR_e$ was relatively similar for these four configurations (fig. 5(a)). However, at 20 mm depth, a relatively moderate increase in $SNR_e$ was obtained by increasing the line density. For example, at 20 mm depth, peak $SNR_e$ increased by 13.3, 14.6, and 18.2% when line density increased by 2, 4, and 8 times, respectively (fig. 5(b)). The corresponding parallel lines, however, increased from 5 to 13, 23, and 45, respectively.

**Using larger transmit aperture (lower F#) resulted in higher $SNR_e$ (fig. 6).**

At the focal depth (25 mm), the maximum $SNR_e$ obtained with F#=1.5 aperture was 116.4% higher than those obtained with F#=5 aperture (fig. 6c). At 20 mm depth, the maximum $SNR_e$ obtained with F#=1.5 aperture was 25.3% higher than those obtained with F#=5 aperture (fig. 6b). At depths shallower than transmit focus, the number of parallel lines that maximizes the $SNR_e$ increased with increasing aperture size (decreasing F#). For example, at 20 mm depth, number of parallel lines that maximized $SNR_e$ increased from 3 to 7 when F# was changed from 5 to 1.5 (fig. 6b). However, at the focal depth, the maximum $SNR_e$ was always obtained using 3 parallel lines irrespective of the transmit F# (fig. 6c). Although parallel beamforming was limited by the transmit beamwidth at focus, it improved the $SNR_e$. For example, with an F#=2.0 aperture, averaging estimates from 3 parallel lines improved the focal zone (25 mm) $SNR_e$ by 40.9% compared to the no averaging case (fig. 6c).

**When a depth-limited ROI was desirable for SWS quantification, placing the tracking focus deeper than the ROI improved the $SNR_e$ (fig. 7).**

Deeper transmit focal zones allowed a larger number of parallel lines for a given quantification region. Peak $SNR_e$ at 15 mm was obtained with 3, 7, 11, and 15 (maximum tested) parallel lines when using 15, 20, 25 and 30 mm tracking focal depths, respectively. Also, the peak $SNR_e$ for 20, 25, and 30 mm transmit focus improved by 9.5, 18.1, and 33%, respectively, compared to the case with 15 mm transmit focus. When the SWS quantification is desirable at a fixed depth, using a deeper tracking focus may enable better performance than pSTL-SWEI.

**Although $SNR_e$ obtained from pSTL-SWEI was higher in most cases, focused STL-SWEI often performed better near the focal region (figs. 8,9).**

In the elastic phantom with lower acoustic attenuation (fig. 8, fig. 9(a)), $SNR_e$ of elastograms obtained using single focus STL-SWEI with no track line averaging was, on average (along the entire depth), 39.7% lower than the corresponding pSTL-SWEI elastograms. Parallel track line averaging (DDA) reduced this difference to 21.9%. The $SNR_e$ was approximately similar near the focal zone. In the elastic phantom with higher acoustic attenuation (fig. 8, fig. 9(b)), $SNR_e$ of focused STL-SWEI (with DDA) elastograms

Author Manuscript Author Manuscript Author Manuscript Author Manuscript

were, on average 39.7% lower than pSTL-SWEI elastograms in the 5 to 15 mm depth range. At the 15 to 20 mm depth range, however, focused STL-SWEI produced 17.4% higher $SNR_e$ than pSTL-SWEI. Beyond 20 mm depth, pSTL-SWEI elastograms were severely degraded in this phantom. In the viscoelastic phantom (fig. 8, fig. 9(c)), pSTL-SWEI produced higher $SNR_e$ than focused STL-SWEI from 5 to 22.5 mm depth. Near the focal region, focused STL-SWEI produced better $SNR_e$ than pSTL-SWEI. When the SWS quantification is desirable at a fixed depth, using a deeper tracking focus may enable comparable performance to pSTL-SWEI. For example, in the phantom with lower acoustic attenuation, it was possible to achieve up to 14.2% higher $SNR_e$ than pSTL-SWEI by increasing the tracking focal depth (fig. 7).

### Parallel beamforming improved $CNR_e$ of inclusion elastograms by reducing the noise variance (figs. 10, 11).

For a focused STL-SWEI acquisition with push and track transmit focus at 15 mm, the $CNR_e$ was 8.68, which was improved by up to 9% and 14.3% when using parallel beamforming with the same (15 mm) and a deeper (25 mm) tracking transmit focus, respectively (fig. 11). The peak $CNR_e$ obtained with focused STL-SWEI (25 mm transmit focus with 15 track line averaging) was 9.6% higher than the peak $CNR_e$ obtained with pSTL-SWEI (with 11 track line averaging).

## V. Discussion

In this work, we evaluated parallel receive beamforming strategies using focused transmit beams to reduce the estimation variance of STL-SWEI. Following key insights resulted from our analysis:

- Off-axis receive positions near the focal zone produced noisy SWS estimates (fig. 2).
- Single focus imaging produced better depth-dependent performance than multi-focal imaging (fig. 4).
- Increasing the receive line density did not improve the maximum $SNR_e$ significantly (fig. 5).
- Large transmit apertures (low F#) produced maximum $SNR_e$; however, the optimum number of parallel lines at the focal zone remained unchanged when F# was varied (fig. 6).
- When SWS quantification is performed at a fixed depth (within push focus, for example), track focus may be placed at deeper regions to reduce the SWS variance through higher level of track line averaging (fig. 7).
- Depth-dependent averaging resulted in optimum depth-dependent $SNR_e$ in single focus imaging (fig. 3).
- Plane wave based STL-SWEI produced better performance than focused STL-SWEI in most cases except near the focal regions (fig. 9).

Author Manuscript Author Manuscript Author Manuscript Author Manuscript

Although plane wave imaging with parallel beamforming reduces the SWS variance of STL-SWEI, it is often not available in clinical scanners. Clinically available scanners usually employ focused transmit beams with parallel beamforming, which has not yet been investigated for STL-SWEI. In this work, we found that parallel beamforming with focused transmit beams can improve the estimation variance (figs. 4, 6). Parallel beamforming, however, strongly depends on the transmit beam shape. We found that, for focused beams, SWS variance significantly increased near the focal zone when the estimates from a large number of parallel beams (>3) were averaged (fig. 6). For B-mode imaging with focused parallel beamforming, this is a well known problem. Nguyen and Prager attempted to mitigate this problem by modeling the beam characteristic in the lateral regions near the focal zone [26], although the effectiveness of this method for wave motion tracking is unknown. Bottenus recently demonstrated an approach to extract element-wise synthetic aperture data from focused transmissions and overcome this limitation [27]. However, the limited number of transmissions (at a given phase of shear wave [19]) may preclude this method's use in SWEI. Parallel beamforming with focused apertures are often supplemented by coherent addition of receive beams from multiple transmissions [28], [29]. Future studies will need to investigate whether coherently compounded receive lines from multiple laterally walked apertures improve the averaging and the estimation variance for STL-SWEI.

Multi-focus imaging produced lower $SNR_e$ than single-focus sequences. Off-axis receive lines obtained using multi-focus produced degraded $SNR_e$ at all depths (fig. 2(b),(d)). Consequently, at the shallow regions (<20 mm), single-focus imaging allowed averaging of a larger number of high quality estimates than multi-focus imaging. Although averaging was limited near the focal region (25 mm) of the single-focus sequence, coherent compounding of four focal pulses resulted higher $SNR_s$ in this region compared to the multi-focal sequence. As a result, the single-focus sequence outperformed multi-focus sequence at most depths in terms of $SNR_e$ (fig. 4). The $SNR_s$ of the multi-focus sequence degraded with depth which was evident from the depth-dependent degradation of $SNR_e$ of the individual receive lines including the on-axis one (fig. 2d). This is likely due to the coherent compounding of lines that are beamformed using the diverging wavefront of the focused transmit. For example, when compounding four beamformed pixels at 25 mm, only one was obtained from the focal zone of a transmit pulse while the remaining pixels were obtained from the post-focal diverging region. Due to the geometric spreading of diverging wave, such post-focal data points have inherently lower $SNR_s$ than focal zone data. Applying depth-dependent lateral masks further exacerbated the condition for the multi-focus sequence. For example, when a depth-dependent mask was applied, the off-axis pixels at the deep regions were primarily obtained from the diverging regions of the shallowest focal pulses. Consequently, applying DDA effectively resulted in a depth-dependent degradation in $SNR_e$ for multi-focus sequences (fig. 4b).

Increasing the line density increased the number of parallel lines within the extent of the transmit beamwidth, but did not improve the $SNR_e$ significantly (fig. 5). As the parallel lines are formed at increasingly closer distances, the noise component in these lines became more correlated. Consequently, the variance in SWS estimates from these lines did not diminish upon averaging. While at regions shallower than focus there was modest improvement in $SNR_e$, significantly larger numbers of lines (up to 45) needed to be averaged to achieve this

Author Manuscript Author Manuscript Author Manuscript Author Manuscript

gain. Thus, for clinical systems with a limited number of parallel receive beamformers, increasing the line density may not be a viable approach to overcome the beamwidth-imposed performance upper limit in the focal region.

It is likely that the improvement in SWS primarily resulted from the averaging of multiple noise realizations rather than the averaging of independent speckle realizations. Offerdahl and McAleavey previously demonstrated that, in STL-SWEI, independent speckle averaging produced only marginally higher reduction in SWS variance than fixed-speckle averaging [30]. Intuitively, this can be explained from the fact that STL-SWEI largely removes the effect of speckle by using a common track location. In our study, we found that closely spaced track lines produced diminishing reduction in SWS variance upon averaging (fig. 5). Although one might speculate that this is related to speckle size relative to track line spacing, this is again related to independent electronic noise realization. When parallel lines are formed at close distances, they sample similar datapoints in the aperture domain during delay-and-sum beamforming. Consequently, parallel beamforming with sufficiently dense lines may produce to partially correlated electronic noise between adjacent parallel lines.

Larger transmit apertures maximized the $SNR_e$ for focused STL-SWEI (fig. 6). For focused beams, the beamwidth increases at the regions shallower than focus when transmit aperture size is increased. Consequently, at shallow regions, larger transmit apertures (low F#) enabled higher level of parallel line averaging which increased the $SNR_e$ (fig. 6a,b). For focal regions, on the other hand, beamwidth decreases with increasing aperture size. However, the maximum $SNR_e$ at the focal region was still obtained using large transmit apertures (low F#) (fig. 6c). This suggests that the $SNR_e$ at the focal region was primarily driven by the higher acoustic energy radiated by larger transmit apertures. Although smaller apertures can potentially enable larger parallel line counts within the focal beamwidth, we did not observe such effect. This is due to the large line spacing (transducer pitch) used in our study. In our study, when the F# was varied from 1.5 to 5, it resulted in a focal beamwidth (= wavelength x F# [31]) between 0.22 mm to 0.77 mm. When five or more parallel lines were beamformed at 0.3 mm spacing, it resulted in a total beam span (>=1.2 mm) that was larger than the focal beamdwidth at any F#. Consequently, using five or more parallel lines always degraded the focal $SNR_e$ irrespective of F#. Using a higher line density could have visualized subtle impacts of transmit F# on the number of parallel lines at the focus. However, relatively minor $SNR_e$ gain at such high line density (fig. 5c) did not warrant such analysis.

In applications where quantification is performed within a limited depth (such as within push beam focal depth), using a deep tracking focus may be beneficial (fig. 7, 11). For B-mode imaging with focused virtual source imaging [32], Kim *et al.* previously demonstrated a similar strategy to overcome the focal beamwidth associated artifacts [33]. In our proposed method, when the focal zone was deeper than the quantification ROI, it enabled a higher level of parallel beam averaging capability due to the wider transmit beam width, resulting in improved peak $SNR_e$. One can also argue in favor of placing the focus at a shallower depth than ROI. Although the diverging wavefront beyond focus will enable more parallel lines, the $SNR_s$ may be lower. The tradeoffs between more more parallel line and lower

Author Manuscript Author Manuscript Author Manuscript Author Manuscript

$SNR_s$ due to geometric spreading should be carefully studied when employing such diverging beams.

Focused STL-SWEI with parallel beamforming performed better than pSTL-SWEI in the deeper region of the phantom with higher acoustic attenuation (fig. 9(b)). The performance gain could be more pronounced when imaging such materials at large depths (>5 cm). Due to the relatively shallow elevation focus (18 mm) of the transducer used in our study, we did not perform such studies. Plane wave based methods require coherent angular compounding to improve $SNR_s$. Generally, a large number of transmissions (up to 71 reported in [34]) are required to achieve $SNR_s$ comparable to focused imaging. Although a large number of compounding angles can be used in SWEI by using push re-transmit [19], it will deteriorate the frame-rate of STL-SWEI. In the viscoelastic material, the focused STL-SWEI with parallel beamforming produced better focal zone $SNR_e$ than pSTL-SWEI (fig. 9(c)). Due to the hourglass shape of the push intensity, the distance between the push beam and the track line is greatest at the push focal depth. Consequently, it is possible that track lines with attenuated shear waves were included in the averaging set of pSTL-SWEI which used a track line averaging of 15. We previously demonstrated that, for viscous materials, averaging may produce sub-optimum performance when track lines over wider distances are included [16]. The focused STL-SWEI with DDA used only three track lines in the focal zone and, consequently, did not suffer from shear attenuation. However, for situations when imaging is performed at the shallow region of a focused beam in a highly viscoelastic medium, a mechanism to discard track lines with attenuated shear waves [35] may need to be adopted.

A limitation of our work is that we have not evaluated a number of beamforming parameters including apodization and dynamic receive F#. The second limitation is that we evaluated the performance of the proposed method at a relatively shallow depth (up to 3 cm). Although the depth we studied is relevant to a number of applications (breast, musculoskeletal, thyroid, vascular, etc.), in deeper tissues (liver, kidney, pancreas, etc.) the focused transmit beams may outperform plane waves due to better penetration. However, for deep tissue applications, effects such as phase abberation and multiple reflection may also corrupt the push beams. Since STL-SWEI relies on the fidelity of push beam shape for SWS reconstruction, these effects may severely impact performance. Using transmit abberation corrections in push beam and tissue harmonic imaging may be beneficial in these applications. Future research should focus on deep tissue applications of high resolution SWEI imaging and translation of STL-SWEI to clinical scenarios.

## VI. Conclusions

In this study, we investigated parallel receive beamforming strategies using focused transmit beams to reduce the SWS estimation variance of STL-SWEI. We found that the best performance with focused transmission can be achieved when parallel lines are beamformed within the spatial extent of the transmit beamwidth. We did not achieve any improvement in image quality by performing multi-focus imaging. Although the focal beamwidth limited the performance of parallel beamforming, using a focal zone deeper than the imaging ROI circumvented this problem. The results indicate that STL-SWEI sequences with low SWS

Author Manuscript Author Manuscript Author Manuscript Author Manuscript

estimation variance can be implemented in clinical systems that rely on focused beam scanning.

## Acknowledgments

This work was supported by National Institute of Health grant R56 EB024320.

## References

[1]. Sarvazyan AP, Rudenko OV, Swanson SD, Fowlkes J, and Emelianov SY, "Shear wave elasticity imaging: a new ultrasonic technology of medical diagnostics," Ultrasound in Medicine & Biology, vol. 24, no. 9, pp. 1419–1435, 1998 [Online]. Available: 10.1016/s0301-5629(98)00110-0 [PubMed: 10385964]

[2]. Bercoff J, Tanter M, and Fink M, "Supersonic shear imaging: a new technique for soft tissue elasticity mapping," IEEE transactions on ultrasonics, ferroelectrics, and frequency control, vol. 51, no. 4, pp. 396–409, 2004.

[3]. Nightingale K, McAleavey S, and Trahey G, "Shear-wave generation using acoustic radiation force: in vivo and ex vivo results," Ultrasound in medicine & biology, vol. 29, no. 12, pp. 1715–1723, 2003. [PubMed: 14698339]

[4]. Ferraioli G, Filice C, Castera L, Choi BI, Sporea I, Wilson SR, Cosgrove D, Dietrich CF, Amy D, Bamber JC, Barr R, Chou Y-H, Ding H, Farrokh A, Friedrich-Rust M, Hall TJ, Nakashima K, Nightingale KR, Palmeri ML, Schafer F, Shiina T, Suzuki S, and Kudo M, "Wfumb guidelines and recommendations for clinical use of ultrasound elastography: Part 3: Liver," Ultrasound in Medicine & Biology, vol. 41, no. 5, pp. 1161–1179, 2015 [Online]. Available: 10.1016/j.ultrasmedbio.2015.03.007 [PubMed: 25800942]

[5]. Barr RG, Cosgrove D, Brock M, Cantisani V, Correas JM, Postema AW, Salomon G, Tsutsumi M, Xu H-X, and Dietrich CF, "Wfumb guidelines and recommendations on the clinical use of ultrasound elastography: Part 5. prostate," Ultrasound in Medicine & Biology, vol. 43, no. 1, pp. 27–48, 2017 [Online]. Available: 10.1016/j.ultrasmedbio.2016.06.020 [PubMed: 27567060]

[6]. Barr RG, Nakashima K, Amy D, Cosgrove D, Farrokh A, Schafer F, Bamber JC, Castera L, Choi BI, Chou Y-H, Dietrich CF, Ding H, Ferraioli G, Filice C, Friedrich-Rust M, Hall TJ, Nightingale KR, Palmeri ML, Shiina T, Suzuki S, Sporea I, Wilson S, and Kudo M, "Wfumb guidelines and recommendations for clinical use of ultrasound elastography: Part 2: Breast," Ultrasound in Medicine & Biology, vol. 41, no. 5, pp. 1148–1160, 2015 [Online]. Available: 10.1016/j.ultrasmedbio.2015.03.008 [PubMed: 25795620]

[7]. Hollender PJ, Rosenzweig SJ, Nightingale KR, and Trahey GE, "Single-and multiple-track-location shear wave and acoustic radiation force impulse imaging: matched comparison of contrast, contrast-to-noise ratio and resolution," Ultrasound in medicine & biology, vol. 41, no. 4, pp. 1043–1057, 2015. [PubMed: 25701531]

[8]. McAleavey SA, Osapoetra LO, and Langdon J, "Shear wave arrival time estimates correlate with local speckle pattern," IEEE transactions on ultrasonics, ferroelectrics, and frequency control, vol. 62, no. 12, pp. 2054–2067, 2015.

[9]. Elegbe EC and McAleavey SA, "Single tracking location methods suppress speckle noise in shear wave velocity estimation," Ultrasonic imaging, vol. 35, no. 2, pp. 109–125, 2013. [PubMed: 23493611]

[10]. Montaldo G, Tanter M, Bercoff J, Benech N, and Fink M, "Coherent plane-wave compounding for very high frame rate ultrasonography and transient elastography," IEEE transactions on ultrasonics, ferroelectrics, and frequency control, vol. 56, no. 3, pp. 489–506, 2009.

[11]. Tiran E, Deffieux T, Correia M, Maresca D, Osmanski B-F, Sieu L-A, Bergel A, Cohen I, Pernot M, and Tanter M, "Multiplane wave imaging increases signal-to-noise ratio in ultrafast ultrasound imaging," Physics in Medicine and Biology, vol. 60, no. 21, pp. 8549–8566, 2015 [Online]. Available: 10.1088/0031-9155/60/21/8549 [PubMed: 26487501]

[12]. Hollender P, Kuo L, Chen V, Eyerly S, Wolf P, and Trahey G, "Scanned 3-d intracardiac arfi and swei for imaging radio-frequency ablation lesions," IEEE Transactions on Ultrasonics,

Author Manuscript Author Manuscript Author Manuscript Author Manuscript

Ferroelectrics, and Frequency Control, vol. 64, no. 7, pp. 1034–1044, 2017 [Online]. Available: 10.1109/tuffc.2017.2692558

[13]. Hollender P, Lipman SL, and Trahey GE, “Three-dimensional single-track-location shear wave elasticity imaging,” IEEE Transactions on Ultrasonics, Ferroelectrics, and Frequency Control, vol. 64, no. 12, pp. 1784–1794, 2017 [Online]. Available: 10.1109/tuffc.2017.2749566

[14]. Hollender P, Palmeri M, and Trahey G, “Single track location shear wave elasticity imaging of the liver with reduced propagation windows,” in Ultrasonics Symposium (IUS), 2016 IEEE International. IEEE, Conference Proceedings, pp. 1–4.

[15]. Hollender P and Trahey G, “Speckle bias as a 3-d offset for the tracking location of shear wave imaging,” in Ultrasonics Symposium (IUS), 2015 IEEE International. IEEE, Conference Proceedings, pp. 1–4.

[16]. Ahmed R, Gerber SA, McAleavey SA, Schifitto G, and Doyley MM, “Plane wave imaging improves single track location shear wave elasticity imaging,” IEEE Transactions on Ultrasonics, Ferroelectrics, and Frequency Control, vol. nil, no. nil, pp. 1–1, 2018 [Online]. Available: 10.1109/tuffc.2018.2842468

[17]. Ahmed R, Ye J, Gerber SA, Linehan DC, and Doyley MM, “Preclinical imaging using single track location shear wave elastography: monitoring the progression of murine pancreatic tumor liver metastasis in vivo,” IEEE Transactions on Medical Imaging, pp. 1–1, 2020. [PubMed: 31135355]

[18]. Boni E, Yu ACH, Freear S, Jensen JA, and Tortoli P, “Ultrasound open platforms for next-generation imaging technique development,” IEEE Transactions on Ultrasonics, Ferroelectrics, and Frequency Control, vol. 65, no. 7, pp. 1078–1092, 7 2018.

[19]. Ahmed R and Doyley MM, “Distributing synthetic focusing over multiple push-detect events enhances shear wave elasticity imaging performance,” IEEE Transactions on Ultrasonics, Ferroelectrics, and Frequency Control, vol. 66, no. 7, pp. 1170–1184, 7 2019.

[20]. Daigle RE, “Ultrasound imaging system with pixel oriented processing,” 10 16 2012, uS Patent 8,287,456.

[21]. Loupas T, Powers J, and Gill RW, “An axial velocity estimator for ultrasound blood flow imaging, based on a full evaluation of the doppler equation by means of a two-dimensional autocorrelation approach,” IEEE Transactions on Ultrasonics, Ferroelectrics, and Frequency Control, vol. 42, no. 4, pp. 672–688, 1995.

[22]. Langdon JH and McAleavey SA, “Real-time single track location ultrasound elasticity imaging using graphic processing units,” in Image and Signal Processing Workshop (WNYISPW), 2014 IEEE Western New York. IEEE, Conference Proceedings, pp. 42–46.

[23]. Rindal OMH, Rodriguez-Molares A, and Austeng A, “A simple, artifact - free, virtual source model,” in 2018 IEEE International Ultrasonics Symposium (IUS) IEEE, 10 2018.

[24]. Jensen JA, “Field: A program for simulating ultrasound systems,” in 10th ORDICBALTIC CONFERENCE ON BIOMEDICAL IMAGING, VOL. 4, SUPPLEMENT 1, PART 1: 351–353. Citeseer, 1996.

[25]. Parker KJ, Ormachea J, Will S, and Hah Z, “Analysis of transient shear wave in lossy media,” Ultrasound in Medicine & Biology, vol. 44, no. 7, pp. 1504–1515, 7 2018. [PubMed: 29706408]

[26]. Nguyen NQ and Prager RW, “High-resolution ultrasound imaging with unified pixel-based beamforming,” IEEE Transactions on Medical Imaging, vol. 35, no. 1, pp. 98–108, 1 2016. [PubMed: 26731794]

[27]. Bottenus N, “Recovery of the complete data set from focused transmit beams,” IEEE Transactions on Ultrasonics, Ferroelectrics, and Frequency Control, vol. 65, no. 1, pp. 30–38, 1 2018.

[28]. Philips E, “Exploring nsight imaging–a totally new architecture for premium ultrasound.”

[29]. Bradley C, “Retrospective transmit beamformation,” Whitepaper ACUSON SC2000^< TM> Volume Imaging Ultrasound System, 2008.

[30]. Offerdahl K and McAleavey S, “Influence of transmit beamforming parameters on image quality in quantitative elastography,” in 2017 IEEE International Ultrasonics Symposium (IUS) IEEE, 9 2017.

[31]. Shung KK, Diagnostic ultrasound: Imaging and blood flow measurements. CRC press, 2015.

Author Manuscript Author Manuscript Author Manuscript Author Manuscript

[32]. Bae M-H and Jeong M-K, “A study of synthetic-aperture imaging with virtual source elements in b-mode ultrasound imaging systems,” IEEE Transactions on Ultrasonics, Ferroelectrics and Frequency Control, vol. 47, no. 6, pp. 1510–1519, 11 2000.

[33]. Kim C, Yoon C, Park J-H, Lee Y, Kim WH, Chang JM, Choi BI, Song T-K, and Yoo Y-M, “Evaluation of ultrasound synthetic aperture imaging using bidirectional pixel-based focusing: Preliminary phantom and in vivo breast study,” IEEE Transactions on Biomedical Engineering, vol. 60, no. 10, pp. 2716–2724, 10 2013. [PubMed: 23686939]

[34]. Montaldo G, Tanter M, Bercoff J, Benech N, and Fink M, “Coherent plane-wave compounding for very high frame rate ultrasonography and transient elastography,” IEEE Transactions on Ultrasonics, Ferroelectrics and Frequency Control, vol. 56, no. 3, p. 489–506, 3 2009 [Online]. Available: 10.1109/TUFFC.2009.1067

[35]. Deffieux T, Gennisson J-L, Larrat B, Fink M, and Tanter M, “The variance of quantitative estimates in shear wave imaging: Theory and experiments,” IEEE Transactions on Ultrasonics, Ferroelectrics and Frequency Control, vol. 59, no. 11, p. nil, 2012 [Online]. Available: 10.1109/tuffc.2012.2472

Author Manuscript Author Manuscript Author Manuscript Author Manuscript

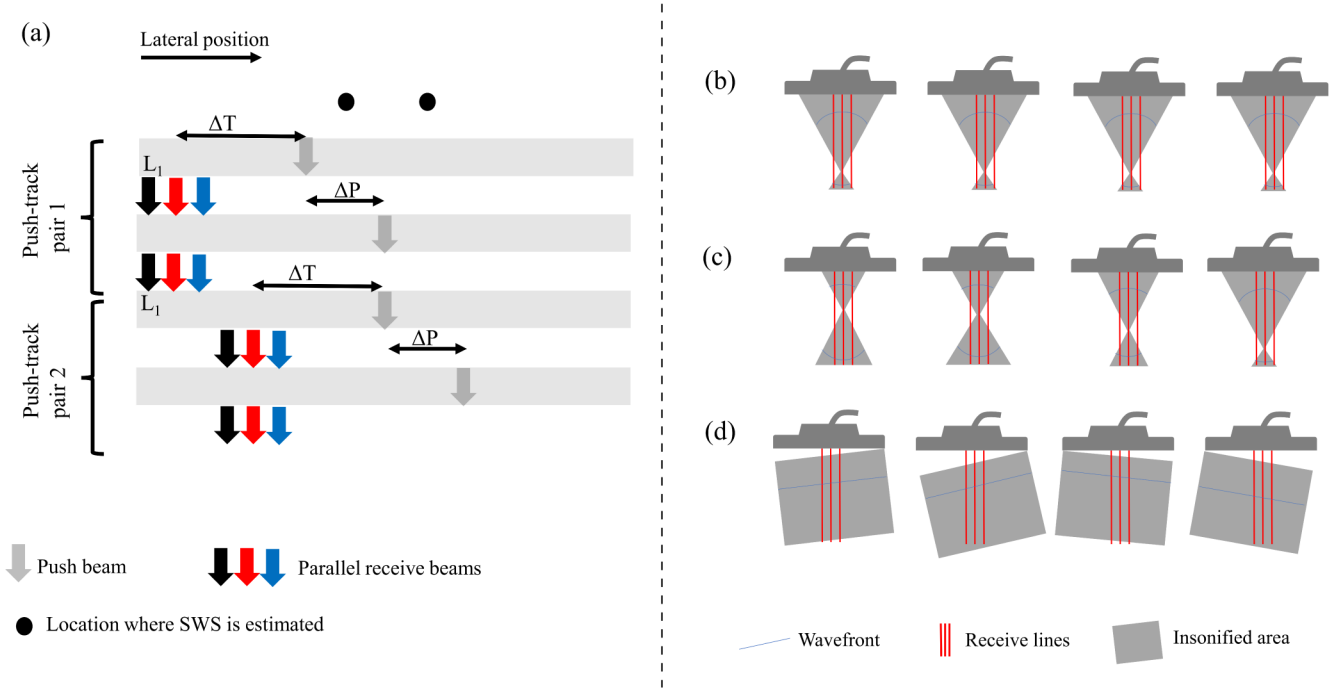


**Fig. 1:**

(a) Pulse sequence of STL-SWEI using parallel receive beamforming. SWS was reconstructed by tracking the shear waves generated from two push beams at a common location. Parallel receive lines were used to track the shear waves at multiple locations simultaneously and the redundant SWS estimates obtained from these parallel locations were averaged. The pair of push-detect ensembles were swept laterally to form a SWS image. The parallel receive lines were reconstructed from either (b) fixed focus, (c) multi-focus or (d) angular plane wave transmissions. Parallel receive lines from four temporally consecutive pulses were coherently summed. In (b), these four pulses were identical. In (c) and (d), they had different focal depths or angular wavefront tilts, respectively.

Author Manuscript Author Manuscript Author Manuscript Author Manuscript

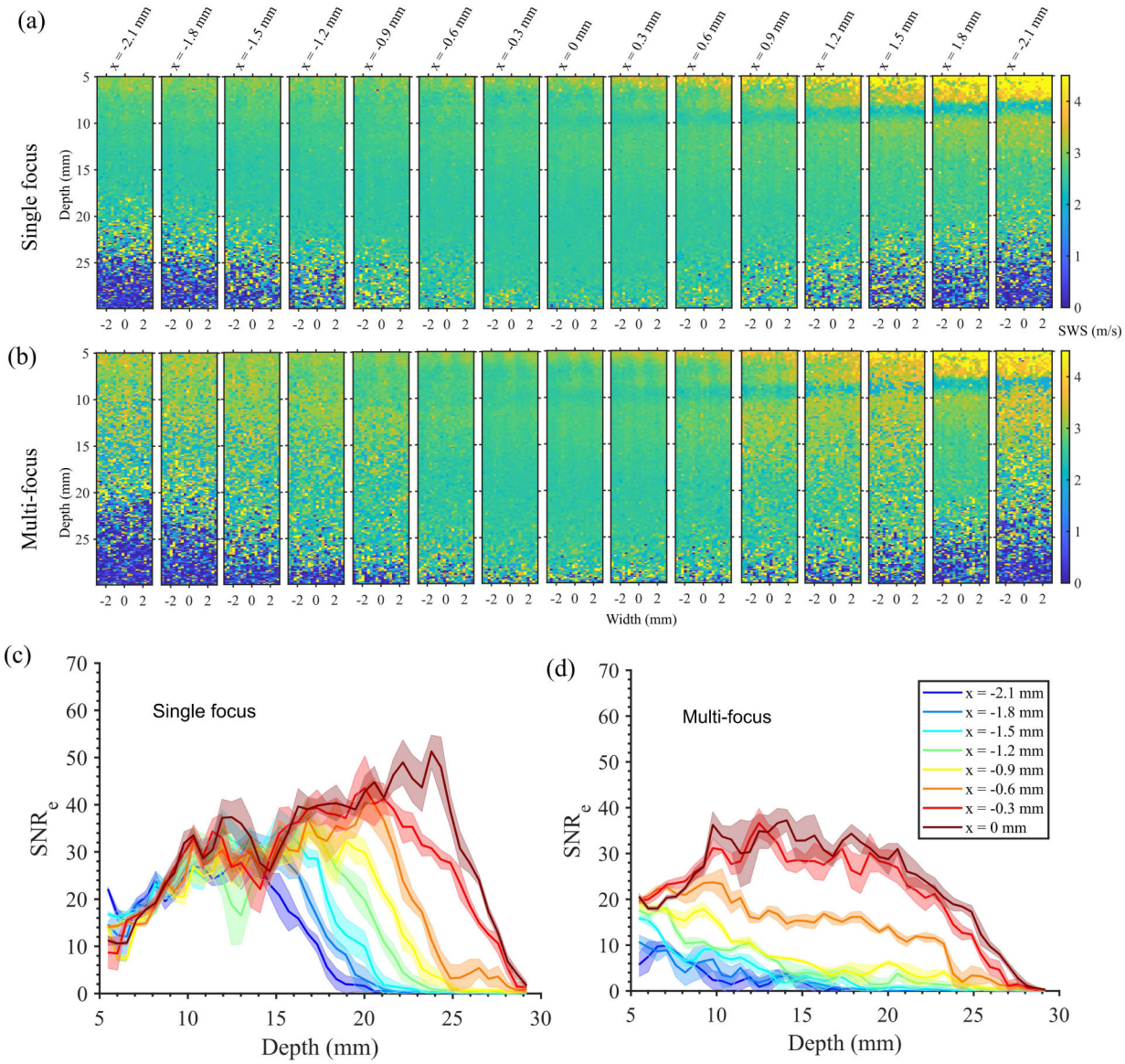


**Fig. 2:**

Quality of SWS estimates as a function of receive beam position. SWS maps obtained from a homogeneous elastic phantom using STL-SWEI with receive beams at different relative positions for (a) single focus and (b) multi-focus transmits. The receive beam position is defined relative to the axis of the transmit beams. The SWS maps are spatially co-registered and are shown prior to averaging. The depth-dependent $SNR_e$ of the SWS maps at different receive beam positions for (c) single focus and (d) multi-focus imaging.

Author Manuscript Author Manuscript Author Manuscript Author Manuscript

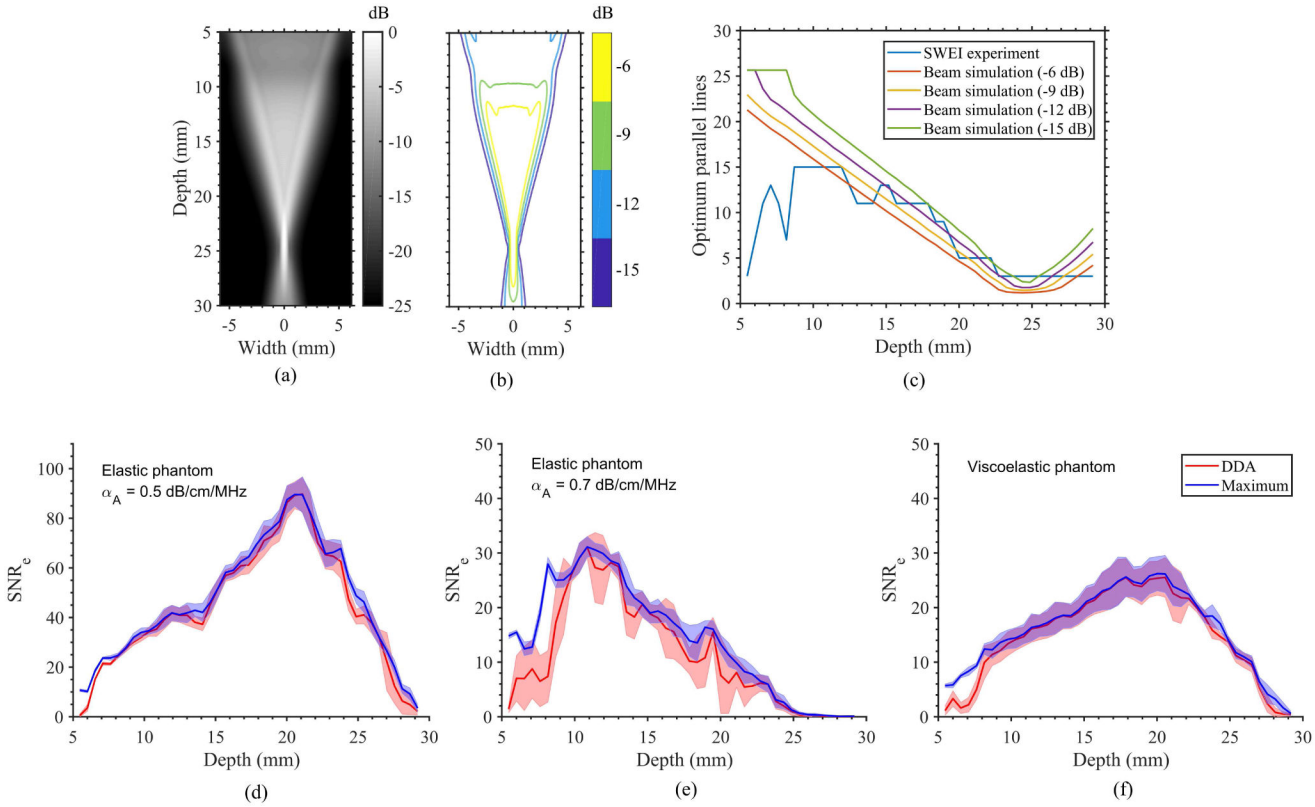


**Fig. 3:**

Depth-dependent averaging based on transmit simulation. (a) and (b) Normalized transmit beam intensity and contour plots, respectively, simulated using FIELD II for an aperture with F#=2.0 in a medium with $\alpha_A$ = 0.5 dB/cm/MHz. (c) Number of parallel lines that maximizes $SNR_e$ (optimum parallel lines) as a function of depth, which were either predicted from different intensity contours or evaluated experimentally on a elastically homogeneous phantom with $\alpha_A$ = 0.5 dB/cm/MHz. (d)-(f) show the depth-dependent $SNR_e$ in three homogeneous phantoms achieved using DDA based on a −12 dB intensity contour. The maximum achievable $SNR_e$ at each depth is also displayed and was computed by evaluating different levels of track line averaging (within a range of 1 to 15). Each line represents a mean over five experiments and the shaded areas represent their standard deviations.

Author Manuscript Author Manuscript Author Manuscript Author Manuscript

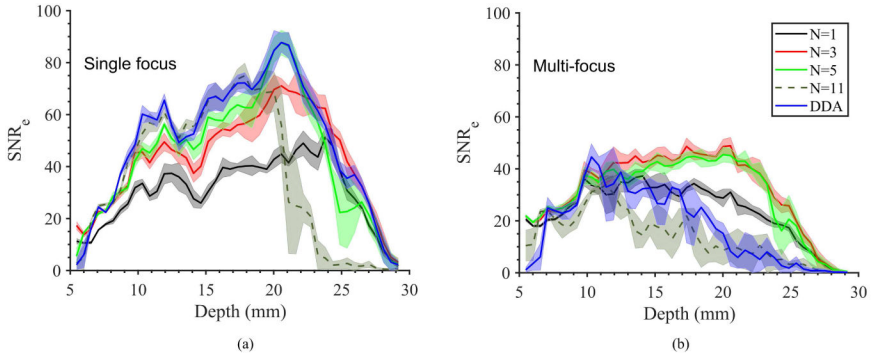


**Fig. 4:**

Comparison of single focus and multi-focus sequences. For both sequences, depth-dependent $SNR_e$ is displayed for different levels of track line averaging (N = 1, 3, 5 and 11) and DDA. Data was acquired from a homogeneous phantom with $\alpha_A$ = 0.5 dB/cm/MHz. Each line represents a mean over five experiments and the shaded areas represent their standard deviations.

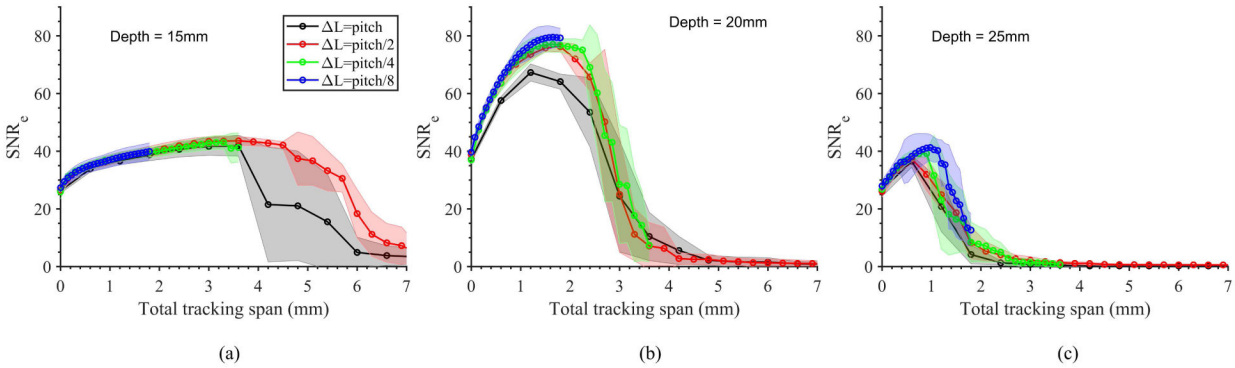


**Fig. 5:**

The impact of beamforming line density on the $SNR_e$ of SWS maps. Data was acquired using single-focus sequence (25 mm focus) and DDA was not applied during processing. The $SNR_e$ is reported as a function of total span of the track lines used in the SWS averaging. $SNR_e$ was evaluated within a 5 mm axial kernel at depths of 15, 20, and 25 mm (focal zone) as shown in the columns left to right, respectively. Results are reported for different beamforming line spacings ($\Delta L$=pitch, pitch/2, pitch/4, and pitch/8). Each line represents a mean over five experiments and the shaded areas represent their standard deviations.



Author Manuscript Author Manuscript Author Manuscript Author Manuscript

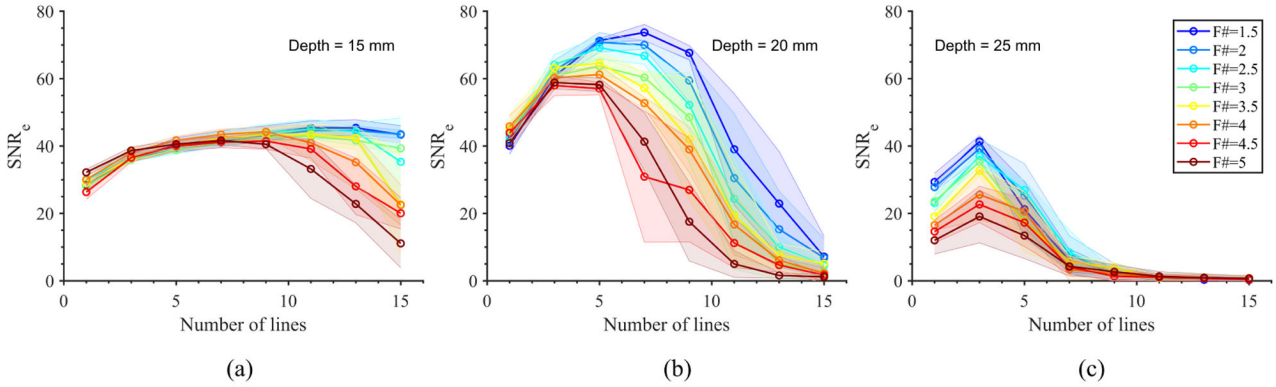


**Fig. 6:**

Effect of averaging level on the $SNR_e$ for different transmit F#. Data was acquired using single-focus sequence (25 mm focus) and DDA was not applied during processing. Results are reported for three different depths. $SNR_e$ was computed using a 5 mm axial kernel. The shaded areas represent standard deviation over five experiments.

Author Manuscript Author Manuscript Author Manuscript Author Manuscript

Author Manuscript Author Manuscript Author Manuscript Author Manuscript

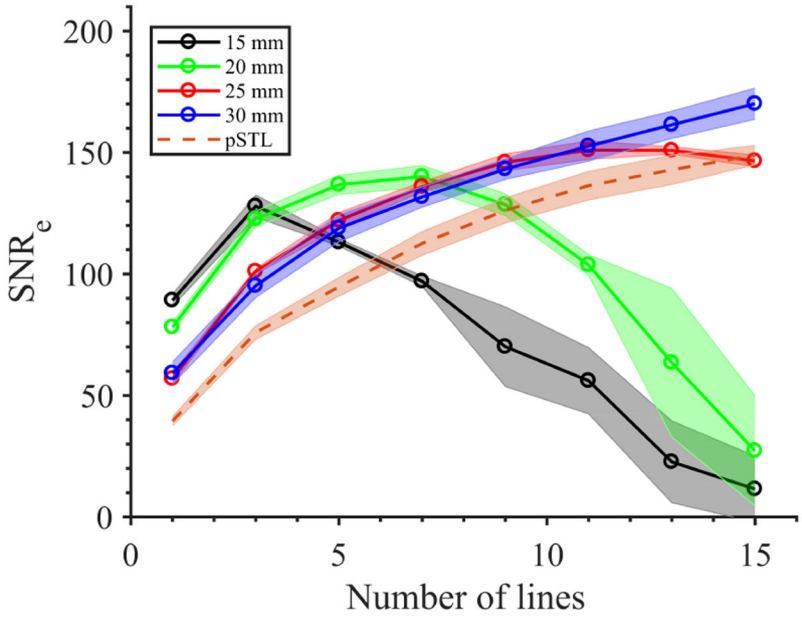


**Fig. 7:**

The impact of using a focal zone deeper than the ROI. $SNR_e$ was evaluated at a fixed depth of 15 mm (within a 5 mm axial kernel) as a function of track line averaging. DDA was not applied during processing and the push beam was focused at 15 mm. Results are shown for single-focus acquisitions with different tracking focal depths (15, 20, 25, and 30 mm) and pSTL-SWEI. The shaded areas represent standard deviation over five experiments.

Author Manuscript Author Manuscript Author Manuscript Author Manuscript

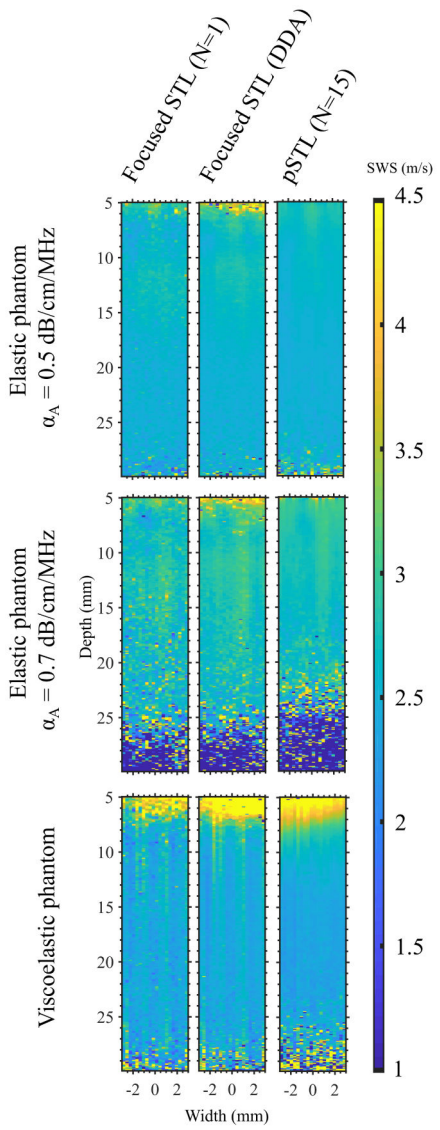


**Fig. 8:**

Elastograms obtained from three homogeneous phantoms using fixed focus STL-SWEI and pSTL-SWEI. First, second and third row show elastograms corresponding to a elastic phantom with $\alpha_A$ = 0.5 dB/cm/MHz, a elastic phantom with $\alpha_A$ = 0.7 dB/cm/MHz, and a viscoelastic phantom, respectively. Columns left to right, represent elastograms obtained using fixed focused STL-SWEI with no track line averaging, DDA, and pSTL-SWEI with 15 track line averaging, respectively.

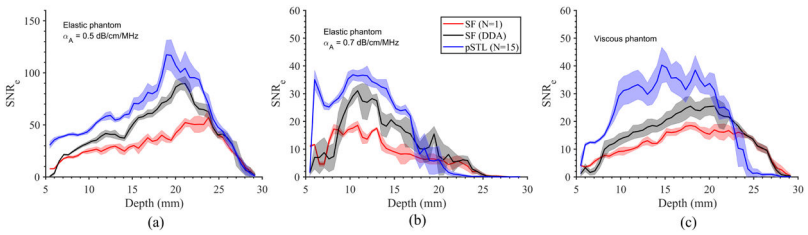


**Fig. 9:**

Comparison of single focus STL-SWEI and pSTL-SWEI in terms of depth-dependent $SNR_e$ computed from elastograms in fig. 8. (a)-(c) show analysis performed using an elastic phantom with $\alpha_A$ = 0.5 dB/cm/MHz, an elastic phantom with $\alpha_A$ = 0.7 dB/cm/MHz, and a viscoelastic phantom, respectively. Shaded areas represent standard deviation over five experiments.

Author Manuscript Author Manuscript Author Manuscript Author Manuscript

Author Manuscript Author Manuscript Author Manuscript Author Manuscript

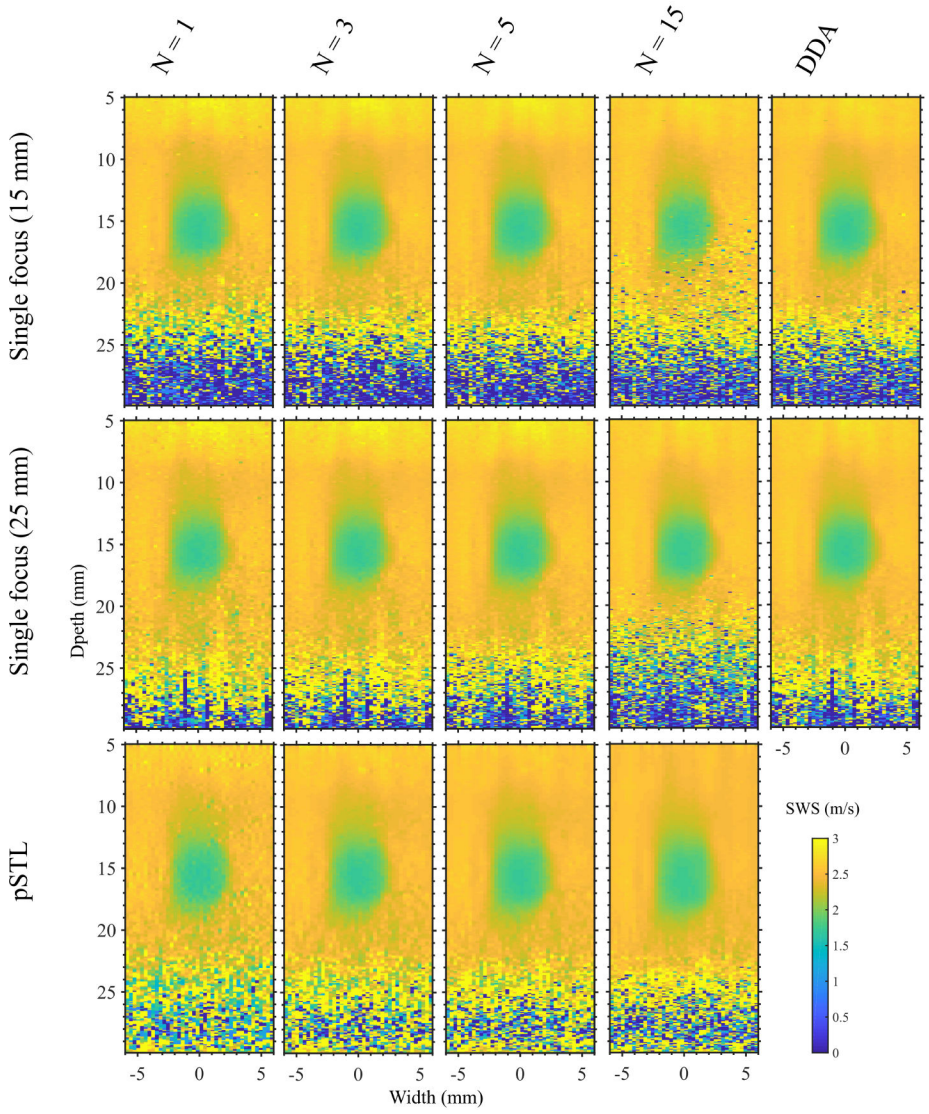


**Fig. 10:**

Elastograms of an inclusion phantom obtained using STL-SWEI and pSTL-SWEI. Elastograms in the rows 1 to 3 were obtained using STL-SWEI with single tracking focus at 15 mm, 25 mm, and pSTL-SWEI, respectively. Elastograms in the columns 1 to 4 were obtained using 1, 3, 5, and 15 track line averaging, respectively. Elastograms in the final column were computed using DDA for the single-focus sequences. In all cases, the push focus was set at 15 mm.

Author Manuscript Author Manuscript Author Manuscript Author Manuscript

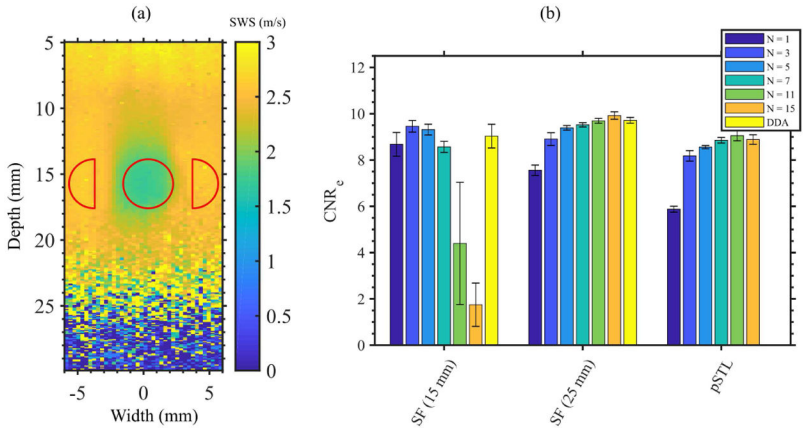


**Fig. 11:**

$CNR_e$ computed from the elastograms in fig. 10. (a) ROI used for the $CNR_e$ calculation. The circular region with 4 mm diameter was used as the inclusion region and the two half-circular regions were used as the background region. (b) $CNR_e$ of STL-SWEI elastograms obtained using STL-SWEI with single focus (SF) at 15 mm, 25 mm, and pSTL-SWEI. For each method, results are shown for 1, 3, 5, 7, 11, 15, and depth-dependent (only for single focus) track line averaging. The errorbars represent standard deviation over five experiments.